

# Mechanics of Continuum Robots with External Loading and General Tendon Routing

D. Caleb Rucker and Robert J. Webster, III

**Abstract** Routing tendons in straight paths along an elastic backbone is a widely used method of actuation for continuum robots. Tendon routing paths which are general curves in space enable a much larger family of robots to be designed, with configuration spaces and workspaces that are unattainable with straight tendon routing. Harnessing general tendon routing to extend the capabilities of continuum robots requires a model for the kinematics and statics of the robot, which is the primary focus of this paper. Our approach is to couple the classical Cosserat theories of strings and rods using a geometrically exact derivation of the distributed loads that the tendons impose along the robot. Experiments demonstrate that the model accurately predicts tip position to 1.7% of the total arc length, on a prototype robot that includes both straight and helical tendon routing and is subject to both point and distributed loads.

## 1 Introduction

Continuum robots offer a number of potential advantages over traditional rigid-link robots in certain applications [1, 2, 3] because of their inherent compliance. Kinematic models which account for deformation due to external loading have been derived for continuum robots with pneumatic actuation [4, 5], multiple flexible parallel backbone tubes [6], and a backbone consisting of concentric, precurved tubes [7, 8]. In this paper, we consider the widely used class of continuum robots actuated by tendons which pass through hollow channels in an elastic structure (e.g. [9, 10, 11]).

Modeling continuum robot shape using continuum mechanics has been the subject of much prior research. Early work by Chirikjian and Burdick in [12, 13] used continuum kinematics and mechanics to model hyperredundant robots. For tendon actuated robots, rod mechanics has been recently applied to obtain free-space kinematic models, as reviewed in [3]. The consensus result is that when the tendons are tensioned, the backbone conforms to a piecewise constant curvature shape. This has been experimentally vetted on a variety of robots (e.g. [9, 14]).

---

D. Caleb Rucker, e-mail: daniel.c.rucker@vanderbilt.edu  
Robert J. Webster III, e-mail: robert.webster@vanderbilt.edu III  
Vanderbilt University, Department of Mechanical Engineering  
101 Olin Hall, 2400 Highland Ave.  
Nashville, TN 37235

In addition to free-space kinematic modeling, some results exist for describing the shape of tendon-actuated continuum robots under external loads. Early theoretical work on the dynamics of a shearless, inextensible rod with general embedded tendons was done by Davis and Hirschorn [15]. Gravagne et al. provide a model in [10, 16] for the statics and dynamics of a planar continuum robot with in-plane loads. Jones et al. [17] applied Cosserat-rod theory to achieve real-time kinematics computations for tendon-actuated robots under external loads, based on the assumption that each tendon applies a point moment at its termination arc length.

In this paper we generalize the Cosserat-rod modeling approach to consider not only the tendon tip moment, but the full set of point and distributed wrenches that a tendon exerts on the backbone structure in its deformed state. To achieve this, we couple the classical Cosserat-rod and string models by expressing the tendon loads in terms of the rod's kinematic variables. This coupled approach allows us to obtain a model for robot designs in which the tendon routing paths are general curves rather than straight and parallel to an initially straight backbone.

The concept and model of general tendon routing expands the design space and the set of shapes achievable for tendon-actuated robots, since the tendon paths themselves can be selected by the designer. Our experimental contribution is the validation of this modeling approach on a physical prototype with straight and helical tendon paths, subject to both distributed and point loads.

## 2 Cosserat-Rod Model

In this section we provide an overview of the classical Cosserat-rod model for our robot backbone. First, let the shape of a rod at rest be defined by a parametric curve in  $\mathbb{R}^3$ ,  $\mathbf{p}^*(s)$ , where  $*$  denotes variables associated with the reference, or at rest, rod shape throughout. We assign reference frames continuously along  $\mathbf{p}^*(s)$  such that their z axes are tangent to the curve. Thus, a continuous homogeneous transformation  $g^*(s)$  is established, consisting of the position and orientation of the reference frame along the curve,

$$g^*(s) = \begin{bmatrix} R^*(s) & \mathbf{p}^*(s) \\ 0 & 1 \end{bmatrix}$$

where  $R^*(s) \in \text{SO}(3)$  is a rotation matrix. One can obtain the local (body frame) twist vector representing how  $g^*(s)$  changes with respect to  $s$  as,

$$\xi^*(s) = [\mathbf{v}^{*T} \mathbf{u}^{*T}] = (g^{*-1}(s)\dot{g}^*(s))^\vee$$

where the dot denotes a derivative with respect to  $s$ . The  $^\vee$  operator here denotes conversion of an element of  $\mathfrak{se}(3)$  to an element of  $\mathbb{R}^6$ . Following the convention of [18], the  $^\vee$  may also indicate the mapping from an element of  $\mathfrak{so}(3)$  (a skew symmetric matrix) to an element of  $\mathbb{R}^3$ . The  $^\wedge$  operator denotes the inverse operation in both cases. Similarly, a deformed curve  $\mathbf{p}(s)$  can be constructed from a deformed twist vector  $\xi(s)$  by integrating the  $\dot{g}(s) = g(s)\hat{\xi}(s)$ , or equivalently,

$$\dot{R}(s) = R(s)\widehat{\mathbf{u}}(s), \quad \dot{\mathbf{p}}(s) = R(s)\mathbf{v}(s) \quad (1)$$

Following [19], the classic rod differential equations below are derived by differentiating the conditions of static equilibrium for an arbitrary section of rod,

$$\dot{\mathbf{n}}(s) + \mathbf{f}(s) = \mathbf{0}, \quad \dot{\mathbf{m}}(s) + \dot{\mathbf{p}}(s) \times \mathbf{n}(s) + \mathbf{l}(s) = \mathbf{0}, \quad (2)$$

where  $\mathbf{f}$  and  $\mathbf{l}$  are applied force and moment distributions per unit of  $s$ , and the internal force and moment vectors are denoted by  $\mathbf{n}$  and  $\mathbf{m}$  respectively. Linear constitutive laws can be used to relate the bending and torsional strains to the internal moments and the shear and elongation strains to the internal forces. If we express the internal moment and force vectors  $\mathbf{m}$  and  $\mathbf{n}$  in global frame coordinates, and the attached frame aligns with the principal axes of a symmetric cross section, we have

$$\mathbf{n}(s) = R(s)D(s)(\mathbf{v}(s) - \mathbf{v}^*(s)), \quad \mathbf{m}(s) = R(s)C(s)(\mathbf{u}(s) - \mathbf{u}^*(s)), \quad (3)$$

where

$$D(s) = \begin{bmatrix} GA(s) & 0 & 0 \\ 0 & GA(s) & 0 \\ 0 & 0 & EA(s) \end{bmatrix}, \quad C(s) = \begin{bmatrix} EI_{xx}(s) & 0 & 0 \\ 0 & EI_{yy}(s) & 0 \\ 0 & 0 & E(I_{xx}(s) + I_{yy}(s)) \end{bmatrix},$$

where  $A(s)$  is the cross sectional area,  $E(s)$  is Young's modulus,  $G(s)$  is the shear modulus, and  $I_{xx}(s)$  and  $I_{yy}(s)$  are the second moments of area about the principal axes, and  $I_{xx}(s) + I_{yy}(s)$  gives the polar moment of inertia about the z-axis. We now express (2) in terms of the kinematic variables using the constitutive laws. Assuming that  $\mathbf{f}$  and  $\mathbf{l}$  are expressed in global coordinates, we use (3), their derivatives, and the kinematic relationships in (1) to expand (2) and solve for the derivatives of the kinematic variables:

$$\begin{aligned} \dot{\mathbf{p}} &= R\mathbf{v} \\ \dot{R} &= R\widehat{\mathbf{u}} \\ \dot{\mathbf{v}} &= \dot{\mathbf{v}}^* - D^{-1} \left( (\widehat{\mathbf{u}}D + \dot{D})(\mathbf{v} - \mathbf{v}^*) + R^T \mathbf{f} \right) \\ \dot{\mathbf{u}} &= \dot{\mathbf{u}}^* - C^{-1} \left( (\widehat{\mathbf{u}}C + \dot{C})(\mathbf{u} - \mathbf{u}^*) + \widehat{\mathbf{v}}D(\mathbf{v} - \mathbf{v}^*) + R^T \mathbf{l} \right) \end{aligned} \quad (4)$$

Thus, we have a system of differential equations ( $\dot{\mathbf{p}}$ ,  $\dot{R}$ ,  $\dot{\mathbf{v}}$ , and  $\dot{\mathbf{u}}$  in terms of  $\mathbf{p}$ ,  $R$ ,  $\mathbf{v}$ ,  $\mathbf{u}$ , and the applied load distributions  $\mathbf{f}$  and  $\mathbf{l}$ ).

### 3 Cosserat-Tendon Model

In this section we use the Cosserat model for extensible strings to describe the tendons and derive the loads that the tendons impose on the backbone. In our derivation, we assume frictionless interaction between the tendons and the channel through

which they travel. We also assume that the locations of the tendons within the cross section of the robot do not change during the deformation. These assumptions are good for designs which use low-friction embedded sleeves or channels, [9], as well as designs which use closely spaced, low-friction standoff disks such as those in our experimental prototype. We separate the terms  $\mathbf{f}$  and  $\mathbf{l}$  in 4 into truly external distributed loads,  $\mathbf{f}_e$  and  $\mathbf{l}_e$ , and distributed loads due to tendon tension,  $\mathbf{f}_t$  and  $\mathbf{l}_t$ .

$$\mathbf{f} = \mathbf{f}_e + \mathbf{f}_t, \quad \mathbf{l} = \mathbf{l}_e + \mathbf{l}_t \quad (5)$$

In order to derive  $\mathbf{f}_t$  and  $\mathbf{l}_t$ , we start by defining the path in which the  $i^{\text{th}}$  tendon is routed along the robot length. The functions  $x_i(s)$  and  $y_i(s)$  give the local coordinates of the tendon as it crosses the x-y plane of the attached backbone frame at  $s$ , and a vector from the origin of the attached frame to the tendon location is then given in attached frame coordinates by

$$\mathbf{r}_i(s) = [x_i(s) \quad y_i(s) \quad 0]^T, \quad (6)$$

as shown in Fig. 1. Then, the space curves defining the undeformed and deformed tendon paths in the global frame are respectively given by

$$\mathbf{p}_i^*(s) = R^*(s)\mathbf{r}_i(s) + \mathbf{p}^*(s) \quad \text{and} \quad \mathbf{p}_i(s) = R(s)\mathbf{r}_i(s) + \mathbf{p}(s). \quad (7)$$

The governing equations for an extensible string are derived by imposing static equilibrium conditions on a finite section of string. This results in the same equation for the internal force derivative as in (2), namely,

$$\dot{\mathbf{n}}_i(s) + \mathbf{f}_i(s) = 0 \quad (8)$$

where  $\mathbf{f}_i(s)$  is the distributed force on the  $i^{\text{th}}$  tendon per unit of  $s$ , and  $\mathbf{n}_i(s)$  is the internal force in the tendon. In contrast to a Cosserat rod, an ideal string can support only tension forces [19], the magnitude of which we denote by  $\tau_i$ . This requires that the internal force be always tangent to the curve  $\mathbf{p}_i(s)$ . Thus, we can write,

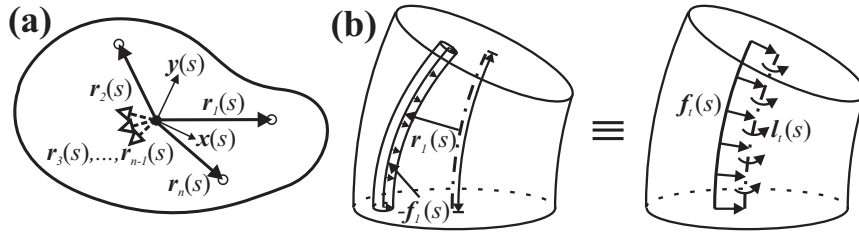


**Fig. 1** (a) General cross section of the continuum robot material or support disk, showing tendon locations. (b) A small section of rod showing how the force distribution that the tendon applies to its surrounding medium is statically equivalent to a combination of force and moment distributions on the backbone itself.

$$\mathbf{n}_i(s) = \tau_i \frac{\dot{\mathbf{p}}_i(s)}{\|\dot{\mathbf{p}}_i(s)\|} \quad (9)$$

where  $\tau_i$  is constant under the frictionless assumption. Using (8) and (9) one can derive the distributed force on the tendon in terms of the tendon path and the tension:

$$\mathbf{f}_i = -\dot{\mathbf{n}}_i = -\tau_i \frac{\dot{\mathbf{p}}_i \times (\ddot{\mathbf{p}}_i \times \dot{\mathbf{p}}_i)}{\|\dot{\mathbf{p}}_i\|^3} = \tau_i \frac{\widehat{\dot{\mathbf{p}}_i}^2}{\|\dot{\mathbf{p}}_i\|^3} \ddot{\mathbf{p}}_i. \quad (10)$$

where we have used the facts that  $\mathbf{a} \times \mathbf{b} = -\mathbf{b} \times \mathbf{a}$ , and  $\mathbf{a} \times \mathbf{b} = \widehat{\mathbf{a}}\mathbf{b}$ .

We now represent the total effect of the tendon loads by a combination of force and moment distributions  $\mathbf{f}_i$  and  $\mathbf{l}_i$  applied at the backbone centroid as shown in Fig. 1 (b). The collective force that all the tendons exert on the backbone is equal and opposite to the sum of the individual force distributions on the tendons (10), and the distributed moment is given by the cross product of the moment arm and the force, namely,

$$\mathbf{f}_t = -\sum_{i=1}^n \mathbf{f}_i \quad \mathbf{l}_t = -\sum_{i=1}^n (\mathbf{p}_i - \mathbf{p}) \times \mathbf{f}_i = -\sum_{i=1}^n (R\mathbf{r}_i)^\wedge \mathbf{f}_i. \quad (11)$$

We now need to express these force and moment distributions in terms of the kinematic variables  $\mathbf{u}$ ,  $\mathbf{v}$ ,  $R$  and  $\mathbf{p}$  in order to substitute them into equation (4). To do this, we must expand  $\dot{\mathbf{p}}_i$  and  $\ddot{\mathbf{p}}_i$ . Differentiating (7) twice yields,

$$\dot{\mathbf{p}}_i = R(\widehat{\mathbf{u}}\mathbf{r}_i + \dot{\mathbf{r}}_i + \mathbf{v}) \quad \ddot{\mathbf{p}}_i = R\left(\widehat{\mathbf{u}}(\widehat{\mathbf{u}}\mathbf{r}_i + \dot{\mathbf{r}}_i + \mathbf{v}) + \widehat{\dot{\mathbf{u}}}\mathbf{r}_i + \widehat{\mathbf{u}}\dot{\mathbf{r}}_i + \ddot{\mathbf{r}}_i + \dot{\mathbf{v}}\right) \quad (12)$$

We note that  $\ddot{\mathbf{p}}$  is a function of  $\dot{\mathbf{u}}$  and  $\dot{\mathbf{v}}$ . Therefore, substituting (12) into (10), and then the loads (11) into the rod model (4) via (5) will yield an implicit formulation of the governing equations for a tendon actuated continuum robot. Fortunately, the resulting equations are linear in  $\dot{\mathbf{u}}$  and  $\dot{\mathbf{v}}$ , and we can therefore express them in explicit form as described in the next section.

## 4 Coupled Rod and Tendon Model

In this section, we rewrite the tendon driven continuum robot model given by (4), (5), (10), (11), and (12) in explicit state-vector form. To express the result concisely, we define some intermediate matrix and vector quantities, starting with (12) expressed in body frame coordinates, namely,

$$\dot{\mathbf{p}}_i^b = \widehat{\mathbf{u}}\mathbf{r}_i + \dot{\mathbf{r}}_i + \mathbf{v} \quad \ddot{\mathbf{p}}_i^b = \widehat{\mathbf{u}}\dot{\mathbf{p}}_i^b + \widehat{\dot{\mathbf{u}}}\mathbf{r}_i + \widehat{\mathbf{u}}\dot{\mathbf{r}}_i + \ddot{\mathbf{r}}_i + \dot{\mathbf{v}}.$$

We define matrices  $A_i$ ,  $A$ ,  $B_i$ , and  $B$ , and vectors  $\mathbf{a}_i$ ,  $\mathbf{a}$ ,  $\mathbf{b}_i$ , and  $\mathbf{b}$  as follows:

$$\begin{aligned}
A_i &= -T_i \frac{(\hat{\mathbf{p}}_i^b)^2}{\|\hat{\mathbf{p}}_i^b\|^3}, & B_i &= \hat{\mathbf{r}}_i A_i, & A &= \sum_{i=1}^n A_i, & B &= \sum_{i=1}^n B_i, \\
\mathbf{a}_i &= A_i (\hat{\mathbf{u}} \hat{\mathbf{p}}_i^b + \hat{\mathbf{u}} \hat{\mathbf{r}}_i + \hat{\mathbf{r}}_i), & \mathbf{b}_i &= \hat{\mathbf{r}}_i \mathbf{a}_i, & \mathbf{a} &= \sum_{i=1}^n \mathbf{a}_i, & \mathbf{b} &= \sum_{i=1}^n \mathbf{b}_i,
\end{aligned}$$

and matrices  $G$  and  $H$  as

$$G = \sum_{i=1}^n [A_i \hat{\mathbf{e}}_1 \mathbf{r}_i \quad A_i \hat{\mathbf{e}}_2 \mathbf{r}_i \quad A_i \hat{\mathbf{e}}_3 \mathbf{r}_i] \quad H = \sum_{i=1}^n [B_i \hat{\mathbf{e}}_1 \mathbf{r}_i \quad B_i \hat{\mathbf{e}}_2 \mathbf{r}_i \quad B_i \hat{\mathbf{e}}_3 \mathbf{r}_i]$$

where  $\mathbf{e}_1$ ,  $\mathbf{e}_2$ , and  $\mathbf{e}_3$  are the standard basis vectors  $[1 \ 0 \ 0]$ ,  $[0 \ 1 \ 0]$ , and  $[0 \ 0 \ 1]$ . Then, we find that  $\mathbf{f}_i$  and  $\mathbf{l}_i$  can be expressed as

$$\mathbf{f}_i = R(\mathbf{a} + A\dot{\mathbf{v}} + G\dot{\mathbf{u}}), \quad \mathbf{l}_i = R(\mathbf{b} + B\dot{\mathbf{v}} + H\dot{\mathbf{u}}).$$

Substituting these tendon load expressions into (4) via (5) and rearranging them, we can now write the governing equations as

$$\begin{aligned}
\dot{\mathbf{p}} &= R\dot{\mathbf{v}} \\
\dot{R} &= R\dot{\mathbf{u}} \\
\begin{bmatrix} \dot{\mathbf{v}} \\ \dot{\mathbf{u}} \end{bmatrix} &= \begin{bmatrix} D+A & G \\ B & C+H \end{bmatrix}^{-1} \begin{bmatrix} D\dot{\mathbf{v}}^* - (\hat{\mathbf{u}}D + \dot{D})(\mathbf{v} - \mathbf{v}^*) - R^T \mathbf{f}_e - \mathbf{a} \\ C\dot{\mathbf{u}}^* - (\hat{\mathbf{u}}C + \dot{C})(\mathbf{u} - \mathbf{u}^*) - \hat{\mathbf{v}}D(\mathbf{v} - \mathbf{v}^*) - R^T \mathbf{l}_e - \mathbf{b} \end{bmatrix} \tag{13}
\end{aligned}$$

Noting that the quantities on the right hand sides of the equations in (13) are functions of  $\mathbf{u}$ ,  $\mathbf{v}$ ,  $R$ ,  $\tau_1, \dots, \tau_n$ ,  $\mathbf{f}_e$  and  $\mathbf{l}_e$ , we have arrived at a system of differential equations in standard explicit form, describing the shape of a continuum robot with any number of embedded tendons and subject to general external loads. The boundary conditions for this system must incorporate the point force  $\mathbf{F}_i$  and moment  $\mathbf{L}_i$  that tendon  $i$  applies at its termination arc length  $\ell_i$ ,

$$\mathbf{F}_i = -\mathbf{n}_i(\ell_i) = \tau_i \frac{\dot{\mathbf{p}}_i(\ell_i)}{\|\dot{\mathbf{p}}_i(\ell_i)\|}, \quad \text{and} \quad \mathbf{L}_i = (R(\ell_i) \mathbf{r}_i(\ell_i))^\wedge \mathbf{F}_i.$$

For example, if a single tendon terminates at the end of the robot ( $s = \ell$ ) and no external point loads are applied, then the distal end boundary conditions would be

$$\mathbf{n}(\ell) = R(\ell)D(\ell)(\mathbf{v}(\ell) - \mathbf{v}^*(\ell)) = \mathbf{F}_1, \quad \mathbf{m}(\ell) = R(\ell)C(\ell)(\mathbf{u}(\ell) - \mathbf{u}^*(\ell)) = \mathbf{L}_1.$$

## 5 Experimental Validation

We performed experiments using the prototype robot shown in Fig. 2 (a). The central backbone is a spring steel rod (ASTM A228) of length  $\ell = 242$  mm and diameter

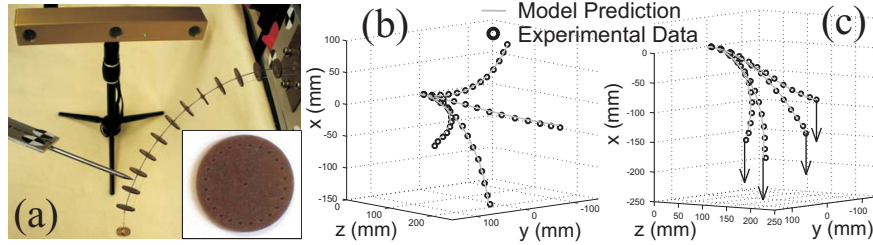


**Fig. 2** (a) Sets of 3D data points along the backbone were taken with an optically tracked stylus. Inset: A standoff disk with a central hole for the backbone rod and outer holes through which tendons may be routed. (b) Model prediction and backbone data are shown when each of the straight tendons are individually tensioned to 2.94 N. The robot sags significantly due to self weight. (c) An additional tip load of 0.098 N is applied.

**Table 1** Tendon Routing Paths used in Experiments

Tendon Number ( $i$ )	1	2	3	4	5
$x_i(s)$ (mm)	8	0	-8	0	$8 \cos(2\pi s/\ell)$
$y_i(s)$ (mm)	0	8	0	-8	$8 \sin(2\pi s/\ell)$

**Table 2** Experimental Tendon Tension and Tip Load Combinations

Individual Tendons Actuated	none	all	all	all	all	1,2,3,4	1,2,3,4	5	5	5
Tendon Load(N)	0	0.98	1.96	2.94	4.91	2.94	2.94	4.91	4.91	6.87
Tip Load(N)	0	0	0	0	0	0.098	0.196	0.098	0.196	0

$d = 0.8$  mm with 12 support disks cut from PTFE filled Delrin plastic to minimize friction with the tendons. As shown in the inset of Fig. 2 (a), 24 small pass-through holes were laser cut in a circular pattern at a radius of 8 mm from the center of each disk. We used 0.36 mm PTFE coated fiberglass thread for the tendons. Table 1 details the location of the tendon routing paths used in our experiments in terms of  $x_i(s)$  and  $y_i(s)$  as defined in (6). We tested 4 straight tendon paths and one helical tendon path where the tendon makes one complete revolution around the backbone. The tendons were tensioned one at a time as detailed in Table 2. Behind the robot base, the tendons were passed over an approximately frictionless pulley and attached to hanging masses (up to 700g). The robot's self-weight, measured to be 0.47 N/m, was enough to cause significant deformation and was incorporated into all model calculations as a distributed force. Also, masses of 10g and 20g were hung from the tip of the robot in selected configurations. A total of 32 experiments were performed, each with an individual tendon tensioned, and some with an additional tip load applied. Table 1 summarizes the tendon tensions and applied loads used in all experiments. In each experiment, a set of 3D backbone data points was collected by manually touching the backbone with the tip of a stylus which was optically tracked using a Micron Tracker 2H3-60 (Claron Technology, Inc.).

## 5.1 Calibration

Because the orientation of the slender robot at its base is difficult to determine directly, and the standoff disks and Loctite adhesive increased the effective stiffness of the backbone, we calibrated the effective Youngs modulus and the set of XYZ Euler angles ( $\alpha$ ,  $\beta$  and  $\gamma$ ) describing the orientation of the base frame. Our calibration process was accomplished by solving an unconstrained nonlinear optimization problem to find the set of parameters which minimizes the sum of the positional errors at the tip of the device. For the parameter set  $P = \{E, \alpha, \beta, \gamma\}$ ,

$$P_{cal} = \underset{P}{\operatorname{argmin}} \left( \sum_{k=1}^{32} e_k \right),$$

where  $e_k = \|\mathbf{p}_{model}(\ell) - \mathbf{p}_{data}(s)\|$  is the euclidean distance between the model tip prediction and the measured tip position in experiment  $k$ .

The nominal parameter set was  $P_{nom} = \{210 \text{ GPa}, 180^\circ, 0^\circ, -90^\circ\}$ , and the calibrated set was  $P_{cal} = \{230 \text{ GPa}, 177.8^\circ, 2.2^\circ, -89.7^\circ\}$ . As expected, the calibrated value of 230 GPa for Youngs modulus was slightly higher than its nominal value of 210 GPa, due to the increased stiffness provided by the disks and glue. Poisson's ratio was held constant at  $\nu = 0.3125$  during calibration so that the shear modulus was correctly scaled relative to Young's modulus.

## 5.2 Results and Analysis

A summary of the tip error statistics for our experiments is given in Table 3 for both parameter sets. With calibrated parameters, the mean tip error over all experiments was 4.0 mm, which corresponds to 1.7% of the total arc length of the robot. Fig. 2 (b) shows the model prediction overlaid on experimental data for four cases where each straight tendon was tensioned to 2.94 N. In Fig. 2 (c) the model and data are shown with an additional 20 g mass hung from the tip of the robot. Similarly, in Fig. 3, the helical tendon is tensioned to 4.91 N and a 20 g mass is hung from the tip. Again, the model predicts the behavior accurately, illustrating our model's capability to account for general tendon routing paths.

**Table 3** Experimental Tip Errors Before / After Calibration

Tip Error Statistic	Straight Path Experiments	Helical Path Experiments	All Exp.	All Exp. % of arc length
mean (mm)	11.4 / 3.6	9.4 / 5.5	10.9 / 4.0	4.5% / <b>1.7%</b>
min (mm)	5.2 / 0.4	3.4 / 1.9	3.4 / 0.4	1.4% / <b>0.2%</b>
max (mm)	17.2 / 8.1	13.2 / 10.0	17.2 / 10.0	7.1% / <b>4.1%</b>
std. dev. (mm)	3.0 / 1.8	3.4 / 2.7	3.2 / 2.1	1.3% / <b>0.9%</b>

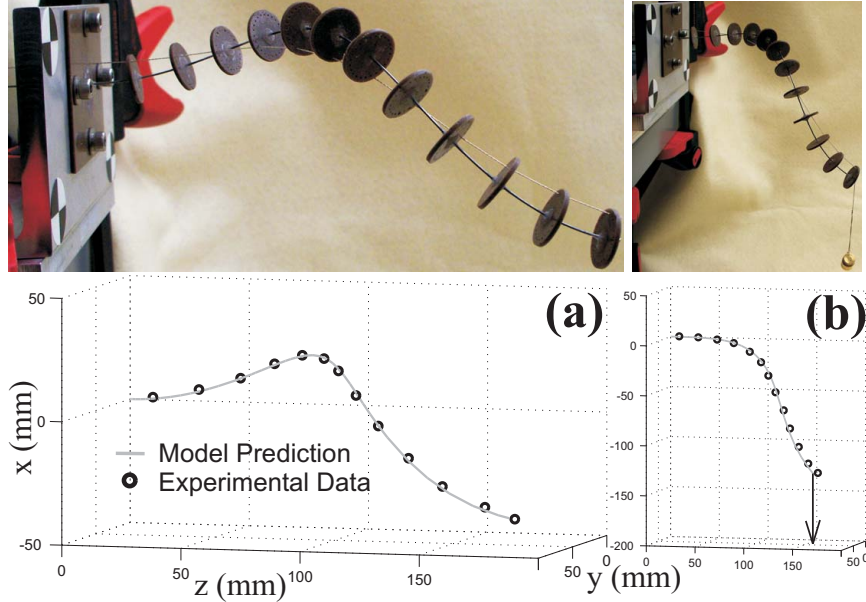


**Fig. 3** (a) A helical tendon is tensioned to 4.91 N. (b) An additional 20 g mass hung from the tip causes large overall deflection. In both cases, the model prediction corresponds well to the measured backbone shape (see Table 3).

The largest source of measurement uncertainty is likely the procedure of manually placing the tip of the stylus on the robot during data capture. We estimate this uncertainty to be at most  $\pm 2$  mm. In general, the largest model errors occurred when the tendons were under the greatest tension, which may be due to unmodeled friction. However, the low overall errors suggest that neglecting static friction is reasonable for our prototype.

## 6 Conclusions

In this paper we have derived an exact model for the forward kinematics and static deformation of continuum robots with general tendon routing, subject to external point and distributed loads. Experimental results demonstrated that using the coupled Cosserat-rod and string approach, one can predict the shape of a physical prototype with both straight and helical tendon paths, under load. With calibrated parameters, the mean Cartesian error at the tip of the robot was 1.7% of the total robot arc length. The model developed in this paper can be useful as a design tool, and for the development of new control algorithms for tendon-actuated continuum robots. Furthermore, the inclusion of general external loads in tendon-actuated continuum robot models is an important step forward for future practical applications, given the

sag exhibited by these robots due to self-weight or payloads. We believe that designs with general tendon routing, and use of models accounting for external loading, will be key enablers of wider application of continuum robots in the future.

## References

1. G. Robinson and J. B. C. Davies, "Continuum robots – a state of the art," *IEEE International Conference on Robotics and Automation*, pp. 2849–2854, 1999.
2. D. Trivedi, C. D. Rahn, W. M. Kierb, and I. D. Walker, "Soft robotics: Biological inspiration, state of the art, and future research," *Applied Bionics and Biomech.*, vol. 5, pp. 99 – 117, 2008.
3. R. J. Webster III and B. A. Jones, "Design and kinematic modeling of constant curvature continuum robots: A review," *Int. J. of Robotics Research*, vol. 29, pp. 1661–1683, 2010.
4. D. Trivedi, A. Lotfi, and C. Rahn, "Geometrically exact models for soft robotic manipulators," *IEEE Transactions on Robotics*, vol. 24, pp. 773 – 780, 2008.
5. J. Wilson and U. Mahajan, "The mechanics of positioning highly flexible manipulator limbs," *J. Mechanisms, Transmissions, Autom. Des.*, vol. 111, pp. 232–237, 1989.
6. K. Xu and N. Simaan, "Analytic formulation for kinematics, statics and shape restoration of multi-backbone continuum robots via elliptic integrals," *ASME Journal of Mechanisms and Robotics*, vol. 2, pp. 011 006–1 to 011 006–13, 2010.
7. D. Rucker, B. Jones, and R. Webster III, "A geometrically exact model for externally loaded concentric-tube continuum robots," *IEEE Trans. on Robotics*, vol. 26, pp. 769–780, 2010.
8. J. Lock, G. Laing, M. Mahvash, and P. E. Dupont, "quasistatic modeling of concentric tube robots with external loads," *IEEE/RSJ International Conference on Intelligent Robots and Systems*, pp. 2325–2332, 2010.
9. D. B. Camarillo, C. F. Milne, C. R. Carlson, M. R. Zinn, and J. K. Salisbury, "Mechanics modeling of tendon-driven continuum manipulators," *IEEE Transactions on Robotics*, vol. 24, no. 6, pp. 1262–1273, 2008.
10. I. A. Gravagne, C. D. Rahn, and I. D. Walker, "Large-deflection dynamics and control for planar continuum robots," *IEEE/ASME Trans. on Mechatronics*, vol. 8, pp. 299–307, 2003.
11. R. Buckingham and A. Graham, "Reaching the unreachable - snake arm robots," *International Symposium of robotics*, 2003, available via OCRobotics Ltd. <http://www.ocrobotics.com>.
12. G. S. Chirikjian, "Hyper-redundant manipulator dynamics: A continuum approximation," *Advanced Robotics*, vol. 9, no. 3, pp. 217–243, 1995.
13. G. S. Chirikjian and J. W. Burdick, "Kinematically optimal hyper-redundant manipulator configurations," *IEEE Transactions on Robotics and Automation*, vol. 11, pp. 794–806, 1995.
14. C. Li and C. D. Rahn, "Design of continuous backbone, cable-driven robots," *ASME Journal of Mechanical Design*, vol. 124, no. 2, pp. 265–271, 2002.
15. J. H. Davis and R. M. Hirschorn, "A model for the embedded tendon control of a slender three-dimensional flexible robot link," *Dynamics and Control*, vol. 4, pp. 185–208, 1994.
16. I. A. Gravagne and I. D. Walker, "Manipulability, force, and compliance analysis for planar continuum robots," *IEEE Trans. on Robotics and Automation*, vol. 18, pp. 263–273, 2002.
17. B. Jones, R. Gray, and K. Turlapati, "Three dimensional statics for continuum robotics," *IEEE/RSJ International Conference on Intelligent Robots and Systems*, pp. 2659–2664, 2009.
18. R. M. Murray, Z. Li, and S. S. Sastry, *A Mathematical Introduction to Robotic Manipulation*. Boca Raton, FL: CRC Press, 1994.
19. S. S. Antman, *Nonlinear Problems of Elasticity*, 2nd ed., S. Antman, J. Marsden, and L. Sirovich, Eds. Springer Science, 2005.